Available online at www.sciencedirect.com
SCIENCE DIRECT®
ELSEVIER
Earth and Planetary Science Letters 211 (2003) 271–286
EPSL
www.elsevier.com/locate/epsl

Seismic and mechanical anisotropy and the past and present deformation of the Australian lithosphere☆

Frederik J. Simons *, Rob D. van der Hilst [1]

Department of Earth, Atmospheric and Planetary Sciences, Masachusetts Institute of Technology, Cambridge, MA 02139, USA

Received 30 September 2002; received in revised form 3 April 2003; accepted 4 April 2003

Abstract

We interpret the three-dimensional seismic wave-speed structure of the Australian upper mantle by comparing its azimuthal anisotropy to estimates of past and present lithospheric deformation. We infer the fossil strain field from the orientation of gravity anomalies relative to topography, bypassing the need to extrapolate crustal measures, and derive the current direction of mantle deformation from present-day plate motion. Our observations provide the depth resolution necessary to distinguish fossil from contemporaneous deformation. The distribution of azimuthal seismic anisotropy is determined from multi-mode surface-wave propagation. Mechanical anisotropy, or the directional variation of isostatic compensation, is a proxy for the fossil strain field and is derived from a spectral coherence analysis of digital gravity and topography data in two wavelength bands. The joint interpretation of seismic and tectonic data resolves a rheological transition in the Australian upper mantle. At depths shallower than ~150–200 km strong seismic anisotropy forms complex patterns. In this regime the seismic fast axes are at large angles to the directions of principal shortening, defining a mechanically coupled crust–mantle lid deformed by orogenic processes dominated by transpression. Here, seismic anisotropy may be considered 'frozen', which suggests that past deformation has left a coherent imprint on much of the lithospheric depth profile. The azimuthal seismic anisotropy below ~200 km is weaker and preferentially aligned with the direction of the rapid motion of the Indo-Australian plate. The alignment of the fast axes with the direction of present-day absolute plate motion is indicative of deformation by simple shear of a dry olivine mantle. Motion expressed in the hot-spot reference frame matches the seismic observations better than the no-net-rotation reference frame. Thus, seismic anisotropy supports the notion that the hot-spot reference frame is the most physically reasonable. Independently from plate motion models, seismic anisotropy can be used to derive a best-fitting direction of overall mantle shear.

Keywords: anisotropy; tomography; deformation; rheology; Australia

* Corresponding author. Present address: Department of Geosciences, Princeton University, Guyot 321B, Princeton, NJ 08544, USA. Tel.: +1-609-258-2598; Fax: +1-609-688-6521. *E-mail address:* fjsimons@alum.mit.edu (F.J. Simons).

☆ Supplementary data associated with this article can be found at 10.1016/S0012-821X(03)00198-5

[1] Present address: Faculteit Aardwetenschappen, Universiteit Utrecht, 3584 CD Utrecht, The Netherlands.

0012-821X/03/$ – see front matter
doi:10.1016/S0012-821X(03)00198-5

1. Introduction

Lattice preferred orientation of anisotropic minerals such as olivine, developed in response to deformation, can produce seismic anisotropy [1]. The orientation of the seismic fast axes relative to the strain directions depends on the deformation mechanism and history, and on rheological variables such as strain rate, stress, temperature and water content [2]. The fast polarization azimuth of seismic waves may align either with the direction of maximum extension (perpendicular to the direction of principal horizontal shortening) [3,4] or with the shear direction (the direction of flow) [5], but the presence of water can change these relationships profoundly [6,7].

Two end-member models are often proposed to explain the origin of seismic anisotropy under continents [8]. The first attributes it to contemporaneous mantle deformation and predicts the fast axes to align with the direction of absolute plate motion (APM) [9–11]. The second assumes coherent deformation of crust and lithosphere throughout their history and predicts that fast axes are parallel to the principal tectonic trends [12–14] – aligned with transpressional and extensional features or perpendicular to the direction of principal horizontal shortening [4], although recrystallization might alter these relationships [15]. Transverse anisotropy with a horizontal symmetry axis is commonly derived from the shear birefringence of body phases [16,17]. The fast polarization directions obtained from such measurements have been compared to the direction of APM [9], to tectonic trends [13], or to predictions from forward models of finite deformation [18–20] to argue the validity of either end-member case or advocate a combination of both.

Laboratory and numerical experiments predict that the rheological regime in the upper mantle depends on many parameters [21]. It has been suggested [22] that a rheological boundary separates fossil lithospheric anisotropy, preserved since the last major orogeny, from current asthenospheric anisotropy due to contemporaneous mantle deformation, which may be consistent with the stratification of the lithosphere suggested by some seismological studies [23,24]. However, the interpretation of seismic layering is diverse [25–27], and the boundary – or transition – between regimes characterized by 'frozen' anisotropy, and 'present-day' lithospheric anisotropy has remained imprecisely mapped.

Resolving this ambiguity requires independent measurements of seismic anisotropy and the dominant past or present strain field responsible for it. However, only in the crust can the strain field likely responsible for seismic anisotropy be observed directly [28]. In the upper mantle, strain orientations are often inferred from surface features such as tectonic trends or from computer simulations of finite deformation. Because the lithosphere is often non-uniformly affected by deformation [29,30], surface trends are poor indicators of the dominant process, however. Furthermore, the depth variation of seismic anisotropy in the upper mantle is difficult to determine. The splitting accumulated by shear waves on near-vertical trajectories represents the unresolved combined effects of fossil anisotropy and contemporaneous mantle deformation and could further be contaminated by anisotropy at any other depth in the mantle [31–34]. Recent studies have made progress in deriving the depth dependence of seismic anisotropy in Australia [35–37], but in the absence of independent measures of strain only qualitative arguments about the contribution of its past and present-day causes could be made.

A last difficulty concerns the mapping of strain in the sublithospheric upper mantle. There, strain is usually derived from the direction of APM, but this depends on the frame of reference [38]. Plate motion expressed in a hot-spot reference frame (HS-APM) [39] will be a good proxy for the mantle strain if the hot spots are indeed stationary with respect to the upper mantle. A no-net-rotation plate motion model (NNR-APM) [40] may reflect mantle strain if certain assumptions about the nature of lithospheric drag are met. Which reference frame best explains the observed seismic anisotropy has remained unresolved [41,42] – although a recent study suggests that the HS-APM most closely matches global observations of long-period surface waves [43].

Here, we use a model based on multi-mode surface-wave propagation to characterize the pattern

of seismic anisotropy as a function of depth (see Section 2 and [37]). In addition, we use the mechanical anisotropy of the lithosphere, defined as the directional dependence in the spectral coherence between gravity anomalies and topography, to infer the principal directions of fossil strain (see Section 3 and [44]). Measuring the angle between the seismic fast axes and the principal compressional directions at different depth intervals allows us to identify the most likely mechanism of deformation, and, in particular, to estimate both the depth to which seismic anisotropy is primarily caused by fossil deformation and the thickness of a coherently deforming crust–mantle lid. Taking plate motion in both the HS and NNR reference frames as a possible proxy for the mantle strain, we study the depth-dependent alignment of the axes of fast polarization with the APM. We interpret the depth range where the alignment is satisfactory to represent a regime where seismic anisotropy is primarily caused by current mantle deformation. Furthermore, we derive an independent best estimate for the motion of the Indo-Australian plate with respect to the underlying mantle.

2. Seismic anisotropy

2.1. Data

The broadband seismic data collected by the Skippy experiment [45] have led to increasingly detailed knowledge of the wave-speed structure of the Australian upper mantle and its anisotropy [35–37,46,47].

The vertical-component seismograms used in this study are from the Skippy portable seismometers and permanent stations operated by IRIS, Geoscope, and AGSO. We selected $\sim$2250 paths, avoiding regions with complex source and mantle structure by considering events along or within the boundaries of the Indo-Australian plate (see [37], their figure 1). We have performed a tomographic inversion for 3-D Earth structure using the method of Nolet [48]. We accounted for variations in crustal thickness and velocity with independent crustal models from broadband receiver functions at each of the stations [49]. Below the crust, our 1-D reference model has shear-wave speeds of 4500 m s^{-1} at 80, 140 and 200 km depth, and 4635 m s^{-1} at 300 km.

The partitioned waveform inversion [48] uses group-velocity filters to isolate fundamental from higher-mode portions of the seismogram, which are fit in different frequency ranges. Where data quality allowed we fitted the fundamental mode between 5 and 25 mHz (40–200 s period) or a narrower frequency band within this range, while the higher modes were fitted between 8 and 50 mHz (20–125 s). With these frequency bounds the fundamental modes can provide sensitivity to structure down to at least 400 km, and, within the limits of our theoretical assumptions, the higher modes yield additional detail [37,47].

2.2. Parameterization

The wave-speed variations are parameterized by means of non-overlapping cells in longitude and latitude, and a combination of triangular and boxcar functions in depth (see Appendix A[2]). The lateral dimension of the equal-area blocks is $2°\times 2°$ (at the equator). This parameterization and the sampling by wave paths define a sensitivity matrix $\mathcal{G}$. In its most concise form the tomographic problem can be expressed as:

$$\mathbf{q} = \mathcal{G}\cdot\mathbf{b} \tag{1}$$

Here, $\mathbf{q}$ is a vector with data constraints, matrix $\mathcal{G}$ is dependent on the path lengths in the surface cells and on their sensitivity to structure at depth, and $\mathbf{b}$ is the vector of unknown coefficients that express the velocity perturbation, $\delta\beta(\mathbf{r})$, on a basis $s_i(\mathbf{r})$ consisting of surface cells and radial interpolating functions, as given by $\delta\beta(\mathbf{r}) = \Sigma_i^N b_i s_i(\mathbf{r})$ (see Appendix A[2]). Eq. 1 represents a linear inverse problem to which we add damping terms and which we solve iteratively. Thus we solve for the 3-D structure in one step, taking into account the individual constraints from all paths and also the radial covariance structure of the 1-D path averages. This distinguishes our approach from the

[2] See the online version of this paper.

one taken by [35]. For a more detailed discussion we refer to [37].

Damping constrains the norm and first gradient of the solution: the deviations from the starting model are conservative and smooth. Our choice of appropriate damping terms is in part motivated by synthetic tests, and validated by comparing trade-off and resolution in a posteriori tests [37].

2.3. Azimuthal anisotropy

Aspherical Earth structure produces variations in seismic wave speed with respect to a 1-D reference model; due to anisotropy, wave speeds will vary dependent on the direction of propagation or on the polarization direction of particle motion (see [50] and references therein). Perturbations to the phase speed of Rayleigh waves due to heterogeneity and slight anisotropy in 3-D structures can be modeled by considering the effect of vertically polarized shear-wave speed deviations in a transversely isotropic reference medium and two elastic constants (G_c and G_s) sensitive to the azimuth (Ψ) of the seismic ray which are zero in isotropic or transversely isotropic media [51]. For slight anisotropy the wave-speed perturbation takes the form:

$$\delta\beta(\mathbf{r}) = \delta\beta_V(\mathbf{r}) + A_1(\mathbf{r})\cos 2\Psi(\mathbf{r}) + A_2(\mathbf{r})\sin 2\Psi(\mathbf{r}) \quad (2)$$

with

$$A_1 = \frac{G_c}{2\rho\beta_V} \text{ and } A_2 = \frac{G_s}{2\rho\beta_V} \quad (3)$$

and with ρ the mass density and, in simplified index notation (C_{ij}) for the elastic tensor (Γ_{ijkl}) [50], $\beta_V^2\rho = L = (C_{44}+C_{55})/2$, $G_c = (C_{55}-C_{44})/2$, and $G_s = C_{54}$. We augment the sensitivity matrix $\mathcal{G}$ of Eq. 1 to include the cosine and the sine of twice the azimuth Ψ of the ray in each surface cell. In the tomographic inversion we will take as a starting point the radial velocity averages that result from the waveform inversion, and solve for heterogeneity ($\delta\beta_V$) and the anisotropic parameters A_1 and A_2. In general, the anisotropic magnitude, $(G_c^2+G_s^2)^{1/2}$, is much harder to resolve than the direction of maximum velocity, $\tan^{-1}(A_2/A_1)/2$ [37].

Equivalent shear-wave splitting directions can be calculated from these depth-dependent elastic constants, assuming the orientation of the fast axes is horizontal. In [37], we showed that the predicted SKS splitting map differs substantially from independent observations [52,53]. Split times are sensitive to the magnitude of anisotropy, which is not well resolved. This explains part of the mismatch between the predicted and the observed splitting parameters, but frequency-dependent effects or the presence of dipping axes of symmetry may also play a role. Resolving depth-dependent anisotropy with body phases is difficult without making a priori assumptions. Hence, we focus the forthcoming interpretation on the results from our surface-wave study as we believe it to be the most direct sample of depth-dependent anisotropy presently available.

2.4. Depth sensitivity

How well surface waves can resolve depth-dependent wave-speed variations is indicated by the sensitivity function of the Rayleigh wave phase speed with respect to elastic perturbations. Fig. 1 depicts an isotropic background model used in the waveform fitting [47] (Fig. 1A) and the associated sensitivities of the (unweighted) sum of all the surface modes making up the seismogram (Fig. 1B,C). In Fig. 1B we focus on the group velocity–frequency range capturing the surface wave proper (the 'fundamental modes'), whereas Fig. 1C shows the sensitivity of the body-wave equivalent modes (the 'higher modes'). Apart from the dependence on density (ρ) and P-wave speed (α) at shallow depths, the sensitivity to perturbations in vertically polarized shear-wave speed (β_V) dominates. Thus, variations in β_V contribute most to the observed waveforms.

The same dominant influence of β_V on the waveform in a realistic anisotropic reference model [23] (Fig. 1D) is obvious from Fig. 1E,F. This motivates the parameterization in terms of β_V, G_c and G_s as in Eqs. 2 and 3.

2.5. Resolution

In [37] we describe several experiments designed to assess the resolution and robustness of our

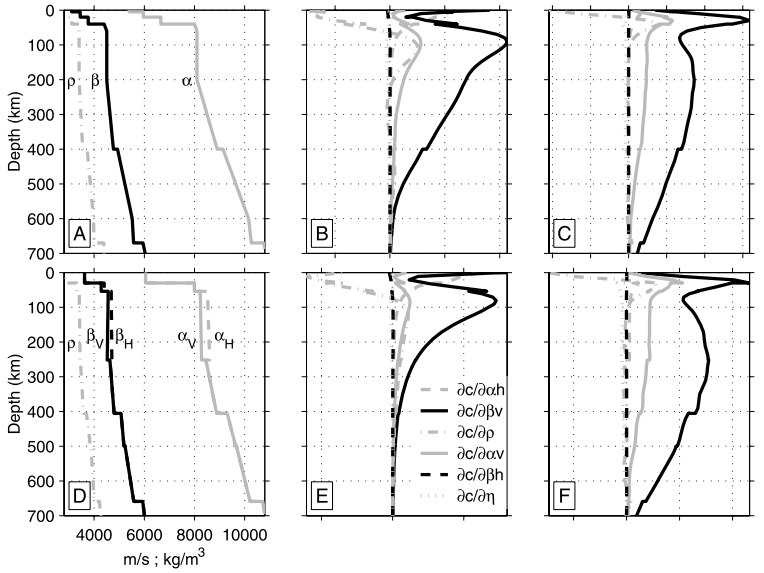

Fig. 1. Earth models and sensitivity kernels of Rayleigh-wave phase speeds. (A,B,C) One of the isotropic reference models used in the waveform inversion of an individual seismogram. The waveform inversion solves for β_V only, using vertical component seismograms. The different modes making up the two analysis windows of the seismogram have phase velocities that are sensitive to perturbations in the elastic parameters according to the Fréchet kernels plotted in panel B (representing predominantly the lower-frequency fundamental mode branch, in the group-velocity range of 3.4–4.4 km/s and frequency range of 5–25 mHz) and panel C (higher modes at higher frequencies, in the range 4.2–4.8 km/s and 8–45 mHz). The dominant partial derivative is the β_V kernel. (D,E,F) Anisotropic model of continental Australia obtained independently by Gaherty and Jordan [23], with the corresponding partials. The same mode selection criterion was used in panels B and E, and panels C and F. For both models and mode windows, the dominant partial is of β_V, which is taken as justification for our parameterization.

anisotropic wave-speed model. With the exception of westernmost Australia, we can retrieve structure on length scales of about 250 km laterally and 50 km in the radial direction, to within 0.8% for the velocity, 20% for the anisotropic magnitude and 20° for its direction.

In addition, we have studied the incremental improvement in variance reduction in our final model due to the inclusion of progressively deeper layers of heterogeneity, anisotropy, or both (see Fig. 2). For the velocity heterogeneity alone, the depth intervals between 30 and 400 km depth contribute most to explain the variance in the data, reaching a plateau of 76.9% for the model between 0 and 400 km and a maximum of 77.5% for the entire depth range of 0–670 km (Fig. 2, *h*). Anisotropy alone between 0 and 400 km only explains 20.1% of the variance in the data, culminating at 20.5% for the entire model between 0 and 670 km (Fig. 2, *a*). The improvement in variance reduction by the addition of successive layers of anisotropy to a model with heterogeneity between 0 and 670 km is from 77.5% to 85.9% at 400 km, culminating at 86.0% for the entire model (Fig. 2, *a*+*h*). Similarly, starting from an anisotropic-only inversion and gradually increasing the allowable depth range of velocity heterogeneity, we improve the 20.5% already explained by anisotropy to the total variance reduction of 86.0% (Fig. 2, *h*+*a*).

Based on these and other arguments [37] we argue that anisotropy forms a valuable addition to wave-speed heterogeneity to explain the deviations from the reference model of the Australian lithosphere, and that both explain the data satisfactorily to a depth of at least 300 km, which is the depth interval we will be using in the interpretations made in this paper.

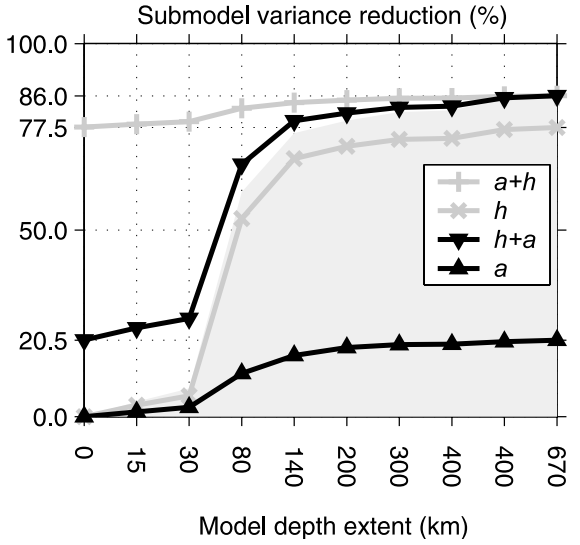

Fig. 2. Data variance reduction of the final model explained progressively in terms of the physical depth range of the model space. The gray area represents the cumulative variance reduction obtained by allowing for wave-speed heterogeneity and azimuthal anisotropy at increasingly larger depths. The curves break this down in terms of heterogeneity only (*h*), which explains the bulk of the data variance; anisotropy added to the entire model of heterogeneity (*a*+*h*), which improves the data fit moderately but significantly; anisotropy alone (*a*), which only explains up to 20% of the data variance; and heterogeneity added to the entire model of anisotropy (*h*+*a*). In all cases, the model range between 15 and 300 km is most responsive to the data; below 300 km little remains to be explained. Other tests have shown that the increase in variance reduction due to the inclusion of anisotropic parameters is significant (see text). Note that our model honors the 400 km discontinuity.

3. Mechanical anisotropy

3.1. The correlation of gravity and topography

The mechanical properties of the lithosphere are reflected in the correlation between Bouguer gravity anomalies and topography. Mountain belts are generally underlain by 'roots' that are less dense than the surrounding mantle. Airy isostasy will cause the Bouguer anomaly to correlate strongly with topography, but for uncompensated topography this will not be the case [54]. In general, the correlation of the Bouguer anomaly to topography is dependent on wavelength. In thick (rigid) lithospheres the transition from highly compensated to uncompensated topography occurs at longer wavelengths than in thin (weaker) plates. When statistically uncorrelated processes simultaneously load and deflect the surface and at least one subsurface lithospheric interface, the spectral coherence function between gravity and topography can be used to invert for an effective elastic thickness T_e or flexural rigidity D, assuming an elastic plate overlying a fluid substrate [55]. In addition to its dependence on a number of elastic parameters the value of T_e further depends on the ratio of surface to subsurface loading (f).

For a model with a single density contrast, $\Delta\rho$, and a subsurface-to-surface loading ratio, f, the predicted Bouguer coherence, γ^2, as a function of the wavenumber, k, is given by:

$$\gamma^2 = \frac{(\xi\Delta\rho^2 + f^2\rho^2\phi)^2}{(\xi^2\Delta\rho^2 + f^2\rho^2)(\Delta\rho^2 + f^2\rho^2\phi^2)} \quad (4)$$

where

$$\xi = 1 + \frac{Dk^4}{\Delta\rho g} \text{ and } \phi = 1 + \frac{Dk^4}{\rho g}$$

In general, f will be a function of wavelength, i.e. $f = f(k)$. It is furthermore influenced by the assumed depth to the loading interface: it includes the effect of the downward continuation of the Bouguer anomaly to such depth (usually taken to equal the Moho discontinuity) [55].

The primary diagnostic to distinguish mechanically weak from strong plates is the transition wavelength at which the change occurs from isostatically compensated (high coherence) to uncompensated loads supported by the elastic strength of the plate (low or zero coherence). To illustrate this we introduce the wavelength $\lambda_{1/2}$ for which $\gamma^2(\lambda_{1/2}) = 0.5$, which can be calculated explicitly. The value of 1/2 is taken for simplicity; in practice we will work with a transition wavelength defined to be the one where the coherence reaches half of its maximum long-wavelength value, which could be different from unity [56]. Note that $\lambda_{1/2}$ is our notational convention; the units of the 'half-wavelength' are in km. The (fourth power of the) transition wavenumber $k_{1/2} = 2\pi/\lambda_{1/2}$ can be determined analytically from Eq. 4:

$$k_{1/2}^4 = \frac{2g}{Df}(-f\Delta\rho - f\rho + f^2\rho + \Delta\rho + \beta^{1/2}) \quad (5)$$

where

$$\beta = f^2\Delta\rho^2 + 4f^2\rho\Delta\rho - 2f^3\rho\Delta\rho + 2f\Delta\rho^2 + f^2\rho^2 + 2f^3\rho^2 - 2f\rho\Delta\rho + f^4\rho^2 + \Delta\rho^2 \quad (6)$$

Eq. 5 illustrates that the ratio of subsurface-to-surface loading f and the rigidity D cannot be determined uniquely, not even in the case where f is independent on wavelength. We thus focus on the behavior of $\lambda_{1/2}$ without attempting to convert this measure into absolute values for the elastic parameters.

3.2. Anisotropy as a record of fossil strain

In most studies the isostatic response function is assumed to be isotropic, i.e. $\lambda_{1/2}$ does not vary with azimuth. Simply stated: a point load (e.g. a mountain) on an elastic plate, compensated to a degree which is a function of the plate strength, will have a cylindrically symmetric deflection associated with it. Similarly, an isotropically compensated line load (e.g. a mountain range) will result in a linear gravity anomaly mimicking the topography. The coherence as a measure of the compensation mechanism represents the average cross-spectral properties of gravity and topography normalized by the individual power spectra of both fields. Thus, regardless of the shape of the power spectrum of either field (e.g. point load or line load), isotropic isostatic compensation will be characterized by a coherence that is circularly symmetric in the wave vector domain: $\gamma^2(\mathbf{k}) = \gamma^2(|\mathbf{k}|) = \gamma^2(k)$.

Many factors might create an elastically anisotropic lithosphere, including, but not limited to, anisotropy in the regional stress field, the banded juxtaposition of lithospheric material with different strengths, parallel fracture zones allowing differential motion in a preferred direction and anisotropy in the subsurface temperature distribution [57]. For such cases the average plate strength could comprise a direction 'stronger' than the isotropic average, and another, 'weaker' direction. The 'weak' direction corresponds to the azimuth in which deformation has accumulated the most and created more than its 'isotropic (average) fair share' of subsurface gravity anomalies given its average strength and the particular topography loading the lithosphere. If there is a dominant direction of weakness in the plate the azimuthally dependent $\lambda_{1/2}(\theta)$ will display a minimum. Hence, on a 2-D estimate of $\gamma^2(\mathbf{k})$ we can determine $\lambda_{1/2}(\theta)$ as a function of the azimuth θ of a profile in wave-vector space.

Measuring anisotropy by mapping out the minimum transition wavelengths is most sensitive to the longer-wavelength portions of the spectrum. Although there is no precise correspondence between the wavelength of the anisotropic coherence anomaly and the depth of the strength anomaly, the longer wavelengths are likely to involve the deeper parts of the elastic lithosphere [54]. A measure of mechanical anisotropy caused by shallower processes can be formed by disregarding the long wavelengths of the coherence. We may extract directional variability from the shorter-wavelength portions of the coherence by comparing the directional average of the short-wavelength coherence to the isotropic average. Both measures identify directions that have accumulated more than the isotropic average of gravitational anomalies for a given amount of topography.

We contend that continental deformation is recorded by topography and gravity anomalies. The coherence function relating them is a wavelength-dependent measure of the amount of flexure experienced by density interfaces in the lithosphere due to loading by a unit of topography. The 2-D nature of the coherence is an expression of the elastic strength or weakness of the plate. The azimuth in which the transition from high to low coherence occurs at the shortest wavelength indicates a direction of mechanical weakness or strain concentration. We thus identify the orientation of preferential isostatic compensation with the direction of abnormally short transition wavelengths (compared to other azimuths) or with the direction of anomalously high average coherence (compared to the isotropic average).

We use coherence anisotropy as a proxy for the lithospheric deformation direction dominant over time and integrated over depth (the 'fossil' strain). This new approach can supplant the limited and

often ambiguous mapping of surface trend directions. Interpreting anisotropic isostatic compensation as a function of the strain directions it records arguably provides a better handle on the dominant deformation mechanism than a surface mapping of geologic trends (strike of faults, province boundaries, stress directions, etc.) alone. Isostatic compensation involves all of the elastic lithosphere, and the isostatic response thus represents the time- and depth-integrated dominant mode of deformation.

If erosion happens in a spectrally isotropic way and the surface and subsurface are in static equilibrium with each other, modest amounts of erosion will not alter the directional relationship of gravity to topography and hence preserve the deformational signature. Severe erosion would invalidate the interpretation of coherence anisotropy due to the anisotropy in the strength of the lithosphere. Alternatively, if the erosion happened under non-equilibrium conditions and the gravity anomalies associated with the previous dominant strain field remained 'frozen' into the lithosphere, the resulting coherence anisotropy, though not reflecting anisotropic strength, would still be a proxy for the fossil strain. We expect more definitive insights into the behavior of gravity, topography and erosion from numerical models.

3.3. Data

Topography and bathymetry data are from the compilation by [44]. Oceanic bathymetry was added to provide continuity with the continental topography. The continental Bouguer gravity anomaly map is from Geoscience Australia (formerly the Australian Geological Survey Organisation); in the construction, a crustal density of 2670 kg m^{-3} was assumed.

A background gravity field obtained from a spherical harmonic expansion of satellite-derived geoidal coefficients up to degree 10 was removed. Over the oceans we computed Bouguer anomalies with a crustal thickness of 6 km [44]. Oceanic and continental data sets were adjusted to the same baseline. The data were projected onto a Cartesian grid with a sampling interval of $\sim$5.5 km in both x and y.

3.4. Measuring coherence

As a concept, 'mechanical anisotropy' is well-documented in the geological literature [44], but although it has been the subject of some investigations by spectral methods, it has only recently been studied with fully 2-D spectral approaches (see [44] and the references therein). The robust and unbiased estimation of coherence functions (depending on space, direction, and wavelength) between two 2-D fields requires specialized techniques. In [44] we estimate the spatially varying coherence between topography and gravity anomalies with a new multi-spectrogram method using orthonormalized Hermite functions as data tapers. Our method optimizes the retrieval of coherence in the spectral domain (the wavelength dependence), the localization of the coherence in the space domain (the spatial dependence), and ensures an isotropic response of the spectral estimator in all azimuths (to get an unbiased estimate of its directional dependence). For a more technical treatment, see [44] and Appendix B[2].

4. Results

4.1. Seismic anisotropy of Australia

Fig. 3A–D shows the heterogeneity and azimuthal anisotropy of the Australian lithosphere obtained from our tomographic inversion of more than 2200 manually processed surface-wave waveforms [37].

As discussed in more detail in Section 2, extensive tests have shown that the level of anisotropy shown in our model is necessary and explains the surface-wave data better than solutions with heterogeneity alone. Although data coverage and resolution degrade from east to west across the continent, the orientation of anisotropy, which is the relevant parameter to our interpretation, is better resolved than its magnitude.

In the top 200 km of the lithosphere the anisotropy is strong, with fast axis orientations highly variable over short length scales, whereas in the bottom 200 km of the model a smoother pattern of slightly weaker anisotropy is observed, in qual-

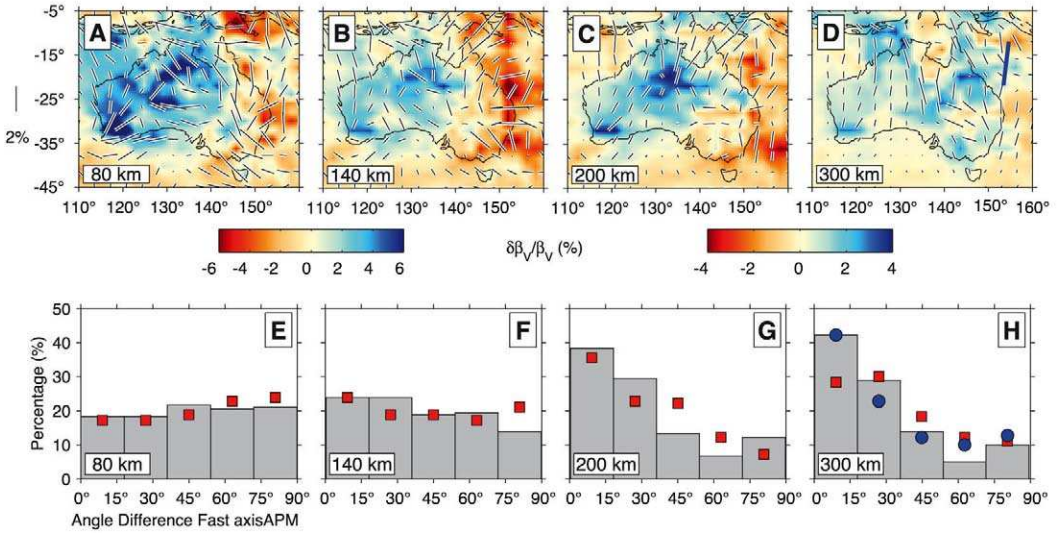

Fig. 3. Seismic structure of the Australian upper mantle and its relation to the motion of the Indo-Australian plate. (A–D) Shear-wave speed anomalies ($\delta\beta_V$) relative to a 1-D reference model (β_V). Black bars: azimuths of fast polarization direction (length proportional to magnitude of anisotropy expressed as a percentage of β_V). (E–H) Histograms of the difference in azimuth of the seismic fast directions with HS-APM (gray bars), with NNR-APM (red squares), and (panel H, blue circles) with our best estimate (panel D, blue bar) of mantle strain at 300 km.

itative agreement with other studies [35]. This observation by itself implies the presence of a rheological transition between 150 and 200 km depth. With increasing depth, a progressively larger proportion of anisotropic fast directions trend with the direction of APM (Fig. 3E,F).

4.2. Tectonic reference frames

The difference between plate motion directions in the HS and NNR reference frames [39,40] approaches 30° in Australia (see Fig. 4). Using synthetic models we investigated if our anisotropic model can distinguish between these frames of reference. In both cases wave-speed heterogeneity identical to our final model at all depths was combined with the anisotropic structure of the final model above 200 km (at the node points of 15, 30, 80 and 140 km). At the nodes centered at 200 and 300 km we input synthetic fast axes exactly aligned with the flow lines in either the HS-APM or the NNR-APM model, with an identical magnitude of 2.2% at both depths. Hence, these synthetic models are representations of the Australian upper mantle in part inspired by the data but with anisotropy perfectly expressing the plate motions at depths of 200 and 300 km. We have created **b** (see Eq. 2) – keeping all information about path coverage and error structure identical (matrix $\mathcal{G}$) we create synthetic observations **q** by a simple matrix multiplication (see Eq. A.3[2]). We treat these synthetic data as we would regular observations. Keeping damping parameters unchanged, we performed inversions for the best-fitting models.

In Fig. 5 we plotted histograms of the difference in angle between the fast axis directions, retrieved after inversion of the synthetic data, and the input flow lines. For the input model with HS plate motion at 200–300 km, the inversion results are shown in Fig. 5a,A. Although the inversion causes some scatter away from the input directions, overall the agreement is very good at both depths. The retrieval of the NNR synthetic data shown in Fig. 5b,B is similarly good.

The bars represent noise-free synthetic data. We then perturb the input data **q** with random noise corresponding to signal-to-noise ratios of 20–dB. Especially at 300 km depth, the fit worsens progressively but not dramatically. Although it is

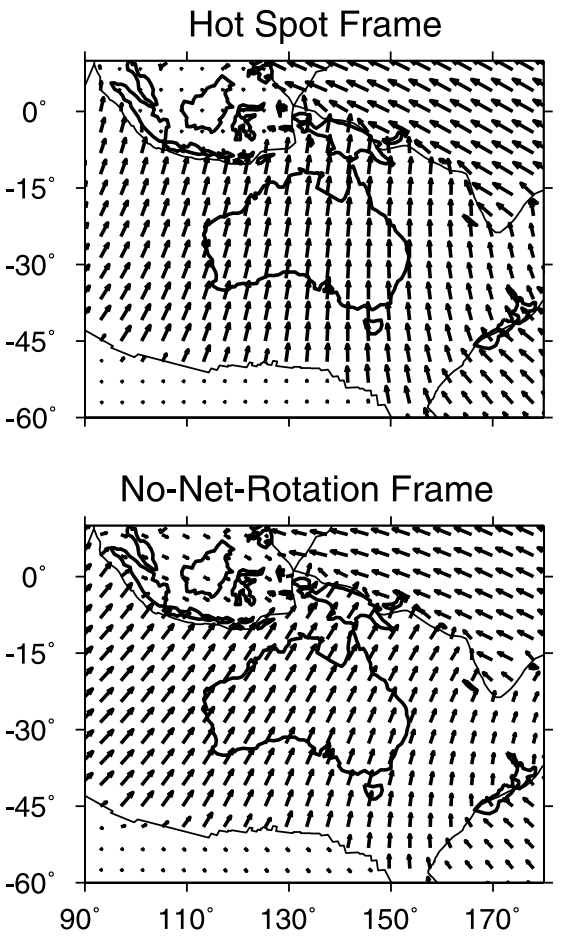

Fig. 4. Motion vectors of the Indo-Australian plate and its surroundings based on the Nuvel-1 model. Current plate velocities are with respect to the hot spots [39] and expressed in a reference frame that yields no net rotation of the plates [40]. Moving at a speed of more than 8 cm/yr, the Indo-Australian plate is one of the fastest moving plates on the planet.

hard to assess the exact noise level of the observed data we conclude that the retrieval of a possible APM signature, whether HS or NNR, holds up very well even with elevated levels of data noise.

We also investigated if we could mistakenly interpret a HS signature as indicative of NNR anisotropy, or vice versa. We illustrate this by plotting histograms of the angular difference between HS plate motion and the results of an inversion with NNR input, in Fig. 5c,C, and between NNR plate motion and an HS inversion in Fig. 5d,D. In all cases, we resolve the mean difference in reference frames of about 25–30° very well, except where the data noise reaches *S*/*N* values of 5–10 dB. These *S*/*N* ratios correspond to a contamination with data noise with energies of 32% and

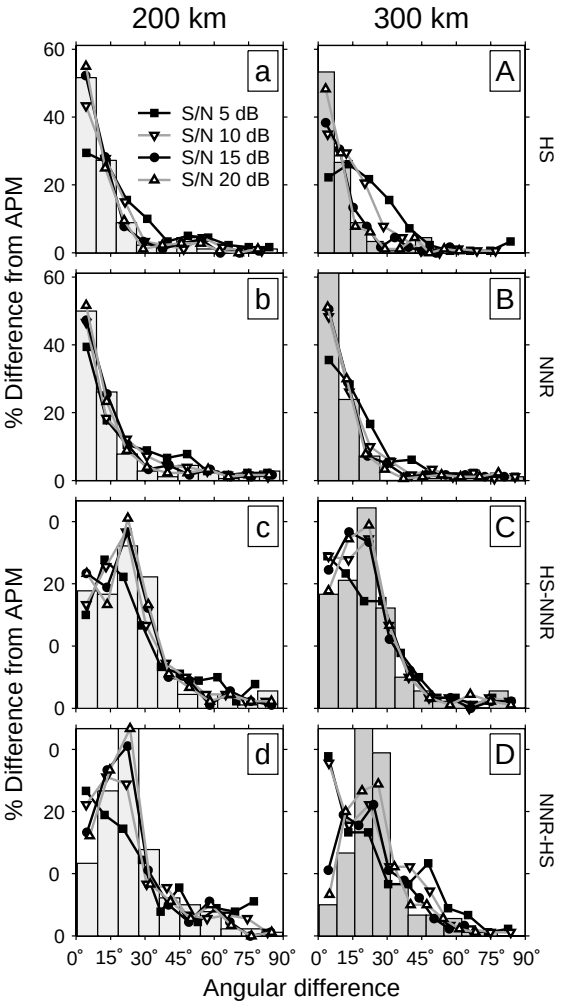

Fig. 5. Summary of the inversion of synthetic data to test whether anisotropic patterns possibly due to current mantle strain derived from two models of plate motion can be retrieved and distinguished from each other. Plotted are the histograms of the difference between input and output anisotropy for the hot-spot (HS; a,A) and no-net-rotation (NNR; b,B) models, and the histograms when the output due to a HS inversion is compared with a NNR model (c,C) and vice versa (d,D). See text for details about the construction of the models. Even with noise added to the data, the top four panels show such hyothetical anisotropy can be well retrieved, while the bottom four panels show they can also be distinguished until the noise level in the data reaches about 10% of the energy in the signal.

10% of the signal energy. We conclude that the difference in plate motion reference frames can be resolved at both depths as long as the data noise does not exceed about 10% of the data, a value which is not likely to be exceeded in our actual data set.

The alignment with the observed seismic anisotropy from surface waves is better explained by APM in the HS-APM than in the NNR-APM. Like Silver and Holt [60], we can also use the seismic anisotropy to derive a direction of mantle shear directly: Fig. 3D shows the constant direction of APM most compatible with our seismic model at 300 km depth by the blue bar oriented at 7° East from North.

4.3. Mechanical anisotropy of Australia

To identify the mechanism responsible for the deformation suggested by the seismic anisotropy we must quantify the relationship between fossil strain and seismic anisotropy in the lithospheric mantle and establish that – on similar length scales – the dominant orientation of deformation is well expressed in the distribution of the fast axes of anisotropy [18,19].

On two-dimensional coherence functions we measure the azimuths with the shortest transition wavelength (Fig. 6A,B) and with anomalously high coherence with respect to the isotropic average (Fig. 6D,E). These 'weak' directions represent the directions of preferential accommodation of deformation ('mechanical anisotropy') in two wavelength regimes. The accuracy of the anisotropy in our coherence estimates is ensured by our multitaper spectrogram technique, which we showed is free of anisotropic bias for realistic loading scenarios [44]. We verified that the difference in coherence between 'strong' and 'weak' directions exceeded the error bars on the measurements and tested the robustness of the directions retrieved under random rotation of our data sets [44]. Only those robust measurements are plotted, and we report no measurements of isotropic coherence. In some cases it was not possible to obtain a stable coherence measurement. This may have a variety of causes [37,56,57], but is most notably due to erosion.

The distribution of weak directions measured from the minima in the transition wavelengths is shown in Fig. 6C, plotted on top of the topography. We summarize the directions with high average coherence in the short-wavelength ($\lambda < 150$ km) portion of the spectrum in Fig. 6F, and plot the gravity anomalies for reference.

5. Discussion

Pronounced high-velocity anomalies suggest that the Australian subcontinental lithospheric keel extends to 225 ± 75 km depth [56]. The pattern of north–south directions of anisotropy observed at 200 and, increasingly, at 300 km suggests that the deepest portion of the lithosphere is deformed by mantle flow associated with the rapid northward motion of the Indo-Australian plate. The large deviations from APM in East Australia, a very well-resolved region [37], where the lithosphere is less than 100 km thick, suggest a complex morphology of the mantle flow around the edge of the Precambrian core of the continent [52], although the detailed geometry of this flow is not constrained by our observations.

The alignment of the seismic fast axes with APM in the hot-spot reference frame suggests that seismic anisotropy below $\sim$200 km is related to present-day mantle deformation. This would imply that dislocation creep is dominant to greater depth than previously thought [23,26], which could be explained by the high stress levels associated with the fast northward motion of the Australian plate [22] or the implied low temperature of the high-velocity lithospheric keel. The observation of a transition zone in wave-speed structure and anisotropy in the range between 150 and 200 km is consistent with those of [25,35] and corroborates certain observations of electrical anisotropy in the Australian lithosphere to first order [41,42]. Measurements of electrical anisotropy sensitive to the depth range >150 km in Central Australia are more closely aligned with NNR-APM than with HS-APM [41,42]. If the discrepancy is significant the obliquity between seismic and electrical anisotropies might have implications for the kinematics of the deformation mech-

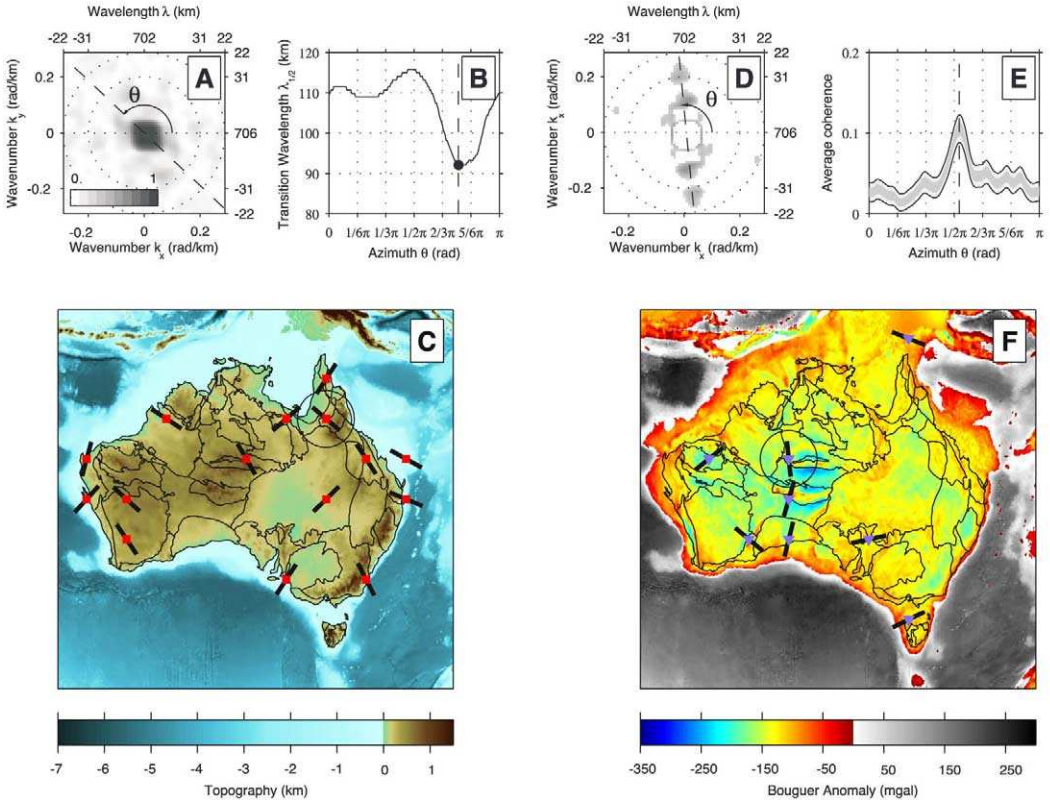

Fig. 6. Mechanical anisotropy of Australia from the relation of gravity anomalies to topography. (A–C) Anisotropy of the long-wavelength portion of the coherence. (A) Coherence and (B) azimuthal variation of transition wavelength of region circled in (C). Direction of preferential isostatic compensation (minimal $\lambda_{1/2}$) dashed in panels A and B; (C, black bars) summary of all measurements. (D–F) Anisotropy of the short-wavelength portion of the coherence. (D) Coherence (long wavelengths omitted from center), and (E) coherence averaged per azimuth (68% and 95% confidence intervals shaded) of region circled in (F). Direction of preferential isostatic compensation (maximal average coherence) dashed in panels D and E; (F, black bars) all measurements. Outlines of main sedimentary basins are plotted as an indication of the gross structural makeup of the Australian continent.

anism [61]. These are, however, beyond the scope of this paper.

The identification of the anisotropy in the depth range below the transition between 150 and 200 km as the expression of current plate motion and the relative success of crustal observations in explaining continental anisotropy [13] justifies the qualitative conclusion that fossil deformation causes the observed anisotropy above the transition occurring between ~150 and 200 km [35].

The deep structure of Central Australia is relatively well studied and the deformation at depth appears to be expressed continuously through the surface [62,63]. In other parts of the continent, however, the correct identification of the dominant strain directions from surface observations is more problematic. There, we can use the orientation of topography and gravity anomalies and determine the depth extent and lateral distribution of the orthogonality of seismic fast axes and principal shortening directions which would be consistent with the strain-controlled behavior often observed in the crust. Our philosophy is akin to the commonly taken approach of evaluating the parallelism of tectonic trends with shear-wave splitting directions. However, in contrast to splitting observations [52,53], surface waves provide

rather detailed information on the depth dependence of anisotropy, and the use of the time- and depth-integrated measure of upper mantle strain provided by the coherence analysis assures we are not interpreting ambiguous crustal tectonic trends as representative of the dominant behavior of the lithosphere.

Fig. 6 shows the location of major geological and geophysical boundaries. Such zones represent substantial rheological heterogeneities. The role of weak zones has been invoked to explain the relative stability of the cratonic parts they circumscribe [58,64]. Most of the mechanical anisotropy shown in Fig. 6 is found outside of the stable continental cratons and is oriented at large angles to the boundaries that separate them. This confirms the notion that such sutures are heavily deformed and mechanically weak [59]. Furthermore, in Central Australia the strong pattern of north–south coherence anisotropy is an expression of the severe north–south orogenic shortening [63] accommodated by a series of east–west running faults cutting deep through the lithosphere with large offsets [65]. The dominant fast axis direction in Central Australia is east–west, i.e. perpendicular to the direction of mechanical anisotropy. Furthermore, several long-wavelength weak directions are oriented at high angles to the ocean–continent boundary. This may be a manifestation of the rheological weakness associated with the junction of oceanic and continental crust [58].

Fig. 7 reveals that above 150–200 km the fast axes of seismic anisotropy are reasonable predictors of the fossil patterns of deformation. More often than not, the fast axes observed at those depths are perpendicular to the weak direction obtained from the analysis of gravity and topography. This relationship to seismic anisotropy is displayed by the weak directions in both the long- (Fig. 7A) and the short-wavelength (Fig. 7B) regime. In both cases the correlation diminishes with increasing depth but the decay is faster for the short-wavelength mechanical anisotropy, as gravity anomalies observed at those scales record shallower processes than long-wavelength ones [66]. Thus, our results suggest that the upper regions of the continental lithosphere, above a transition occurring at $\sim$150–200 km, behave as a mechanically coherent lid. Below 200 km, we do not detect signal from fossil deformation.

6. Conclusions

Our surface-wave tomography and analysis of gravity–topography coherence provide indepen-

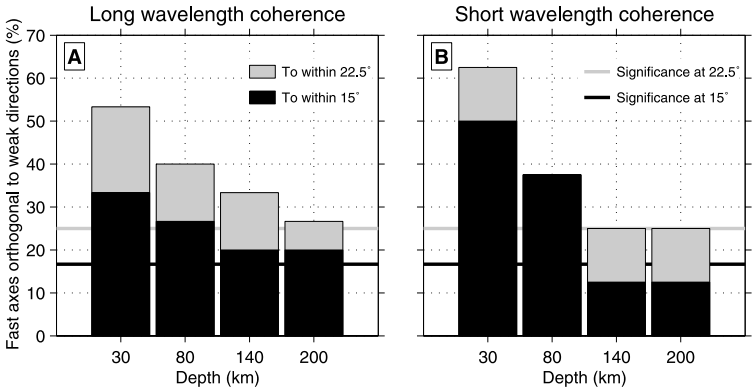

Fig. 7. Angular relationship between seismic anisotropy and fossil deformation of the lithosphere. Are the seismic fast axes (from Fig. 3) perpendicular to the mechanically weak directions (from Fig. 6) as expected from the fossil anisotropy model [12]? Shown is the percentage of fast axes that match the weak direction to within 15° (black) and, where different, to within 22.5° (gray), based on the long-wavelength (A; data from Fig. 6C) and on the short-wavelength parts of the coherence function (B; data from Fig. 6F). Lines indicate levels which would be reached if the angular differences were uniformly distributed. The diminishing correlation between seismic anisotropy and mechanically weak directions betrays the signature of fossil deformation coherently affecting the lithosphere down to 150–200 km.

dent measures of elastic anisotropy and strain in the lithospheric upper mantle. The depth variation of their relation answers questions about continental rheology previously inferred on the basis of incomplete data. We have resolved a change both in the character of seismic anisotropy and in its relation to strain in the depth interval between 150 and 200 km in the Australian subcontinental lithospheric mantle. The angles between the fast axes of seismic anisotropy and the principal shortening directions above 150–200 km argue for a deformation mechanism that produced moderate strain due to horizontal pure shear [4,14]. Hence, the top 150–200 km of the Australian lithosphere primarily records the coherent signature of past deformation episodes. Below 200 km, active processes related to current plate motion provide the dominant explanation for the observed seismic anisotropy. The alignment of the fast axes in the flow direction is consistent with the deformation of a dry olivine mantle [6] by simple shear [11]. The depth range of this alignment is consistent with the pressures and temperatures associated with plastic flow by dislocation creep [5]. The correspondence between seismic fast axes and plate motion of Australia is best when the latter is expressed in a hot-spot reference frame, which demonstrates that seismic anisotropy can add information on plate motion with respect to the underlying mantle that is independent from geodetic and plate-circuit constraints. The correspondence of seismically derived mantle strain with plate motion directions in the hot-spot reference frame implies that hot spots constitute a suitably stationary reference frame and that uniform lithospheric drag models for the mantle strain based on the no-net-rotation frame are unwarranted. Our joint interpretation of seismic and tectonic data can add unique constraints on the rheology and deformation of continents such as North America, in particular when data from Earthscope and USArray [67] become available.

7. References cited in the Appendices

[68,69,70,71,72,73]

Acknowledgements

We thank Greg Houseman, Scott King, W. Jason Morgan, and two anonymous reviewers for their constructive comments on the submitted manuscript. This research was supported by NSF Grant EAR-0001136.*[SK][KF]*

References

[1] J. Park, V. Levin, Seismic anisotropy: Tracing plate dynamics in the mantle, Science 296 (2002) 485–489.
[2] S. Karato, P. Wu, Rheology of the upper mantle: A synthesis, Science 260 (1993) 771–778.
[3] H.R. Wenk, K. Bennett, G.R. Canova, A. Molinari, Modeling plastic-deformation of peridotite with the self-consistent theory, J. Geophys. Res. 96 (1991) 8337–8349.
[4] N.M. Ribe, On the relation between seismic anisotropy and finite strain, J. Geophys. Res. 97 (1992) 8737–8747.
[5] S.Q. Zhang, S. Karato, Lattice preferred orientation of olivine aggregates deformed in simple shear, Nature 375 (1995) 774–777.
[6] H. Jung, S. Karato, Water-induced fabric transitions in olivine, Science 293 (2001) 1460–1463.
[7] E. Kaminski, The influence of water on the development of lattice preferred orientation in olivine aggregates, Geophys. Res. Lett. 29 (2002) 1576, 10.1029/2002GL014710.
[8] P.G. Silver, Seismic anisotropy beneath the continents: Probing the depths of geology, Annu. Rev. Earth Planet. Sci. 24 (1996) 385–432.
[9] L.P. Vinnik, L.I. Makeyeva, A. Milev, A.Y. Usenko, Global patterns of azimuthal anisotropy and deformations in the continental mantle, Geophys. J. Int. 111 (1992) 433–447.
[10] L.P. Vinnik, R.W.E. Green, L.O. Nicolaysen, Recent deformations of the deep continental root beneath southern Africa, Nature 375 (1995) 50–52.
[11] A. Tommasi, Forward modeling of the development of seismic anisotropy in the uppper mantle, Earth Planet. Sci. Lett. 160 (1998) 1–13.
[12] P.G. Silver, W.W. Chan, Implications for continental structure and evolution from seismic anisotropy, Nature 335 (1988) 34–39.
[13] P.G. Silver, W. Chan, Shear-wave splitting and subcontinental mantle deformation, J. Geophys. Res. 96 (1991) 16429–16454.
[14] A. Tommasi, B. Tikoff, A. Vauchez, Upper mantle tectonics: Three-dimensional deformation, olivine crystallographic fabrics and seismic properties, Earth Planet. Sci. Lett. 168 (1999) 173–186.
[15] E. Kaminski, N.M. Ribe, A kinematic model for recrystallization and texture development in olivine polycrystals, Earth Planet. Sci. Lett. 189 (2001) 253–267.
[16] M.K. Savage, Seismic anisotropy and mantle deforma-

tion: What have we learned from shear wave splitting?, Rev. Geophys. 37 (1999) 65–106.
[17] J.-M. Kendall, Seismic anisotropy in the boundary layers of the mantle, in: S. Karato, A. Forte, R. Liebermann, G. Masters, L. Stixrude (Eds.), Earth's Deep Interior. Mineral Physics and Tomography from the Atomic to the Global Scale, AGU Geoph. Monogr. 117, Washington, DC, 2000, pp. 133–159.
[18] P. Davis, P. England, G. Houseman, Comparison of shear wave splitting and finite strain from the India-Asia collision zone, J. Geophys. Res. 102 (1997) 27511–27522.
[19] D.-A. Griot, J.-P. Montagner, Confrontation of mantle seismic anisotropy with two extreme models of strain, in Central Asia, Geophys. Res. Lett. 25 (1998) 1447–1450.
[20] M.J. Fouch, K.M. Fischer, E.M. Parmentier, M.E. Wysession, T.J. Clarke, Shear wave splitting, continental keels, and patterns of mantle flow, J. Geophys. Res. 105 (2000) 6255–6275.
[21] J. Braun, J. Chéry, A. Poliakov, D. Mainprice, A. Vauchez, A. Tommasi, M. Daignières, A simple parameterization of strain localization in the ductile regime due to grain size reduction: A case study for olivine, J. Geophys. Res. 104 (1999) 25167–25181.
[22] S. Karato, On the Lehmann discontinuity, Geophys. Res. Lett. 22 (1992) 2255–2258.
[23] J.B. Gaherty, T.H. Jordan, Lehmann discontinuity as the base of an anisotropic layer beneath continents, Science 268 (1995) 1468–1471.
[24] Y.J. Gu, A.M. Dziewonski, G. Ekström, Preferential detection of the Lehmann discontinuity beneath continents, Geophys. Res. Lett. 28 (2001) 4655–4658.
[25] J.H. Leven, I. Jackson, A.E. Ringwood, Upper mantle seismic anisotropy and lithospheric decoupling, Nature 289 (1981) 234–239.
[26] J. Revenaugh, T.H. Jordan, Mantle layering from *ScS* reverberations. 3. The upper mantle, J. Geophys. Res. 96 (1991) 19781–19810.
[27] B. Romanowicz, Y. Gung, Superplumes from the core-mantle boundary to the lithosphere: Implications for heat flux, Science 296 (2002) 513–516.
[28] M. Scherwath, T. Stern, A. Melhuish, P. Molnar, Pn anisotropy and distributed upper mantle deformation associated with a continental transform fault, Geophys. Res. Lett. 29 (2002) 1175, 10.1029/2001GL014179.
[29] B.R. Goleby, R.D. Shaw, C. Wright, B.L.N. Kennett, Geophysical evidence for 'thick-skinned' crustal deformation in central Australia, Nature 337 (1989) 325–330.
[30] S.B. Lucas, A. Green, Z. Hajnal, D. White, J. Lewry, K. Ashton, W. Weber, R. Clowes, Deep seismic profile across a Proterozoic collision zone: Surprises at depth, Nature 363 (1993) 339–342.
[31] C. Tong, Ó. Guðmundsson, B.L.N. Kennett, Shear wave splitting in refracted waves returned from the upper mantle transition zone beneath northern Australia, J. Geophys. Res. 99 (1994) 15783–15797.
[32] J.-M. Kendall, P.G. Silver, Constraints from seismic anisotropy on the nature of the lowermost mantle, Nature 381 (1996) 409–412.
[33] J. Trampert, H.J. van Heijst, Global azimuthal anistropy in the transition zone, Science 296 (2002) 197–1299.
[34] J. Wookey, J.-M. Kendall, G. Barruol, Mid-mantle deformation inferred from seismic anisotropy, Nature 415 (2002) 777–780.
[35] E. Debayle, B.L.N. Kennett, The Australian continental upper mantle: Structure and deformation inferred from surface waves, J. Geophys. Res. 105 (2000) 25423–25450.
[36] E. Debayle, B.L.N. Kennett, Anisotropy in the Australasian upper mantle from Love and Rayleigh waveform inversion, Earth Planet. Sci. Lett. 184 (2000) 339–351.
[37] F.J. Simons, R.D. van der Hilst, J.-P. Montagner, A. Zielhuis, Multimode Rayleigh wave inversion for heterogeneity and azimuthal anisotropy of the Australian upper mantle, Geophys. J. Int. 151 (2002) 738–754.
[38] A. Kubo, Y. Hiramatsu, On presence of seismic anisotropy in the asthenosphere beneath continents and its dependence on plate velocity: Significance of reference frame selection, Pure Appl. Geophys. 151 (1998) 281–303.
[39] A.E. Gripp, R.G. Gordon, Current plate velocities relative to the hotspots incorporating the Nuvel-1 global plate motion model, Geophys. Res. Lett. 17 (1990) 1109–1112.
[40] D.F. Argus, R.G. Gordon, No-net-rotation model of current plate velocities incorporating plate motion model Nuvel-1, Geophys. Res. Lett. 18 (1991) 2039–2042.
[41] F. Simpson, Resistance to mantle flow inferred from the electromagnetic strike of the Australian upper mantle, Nature 412 (2001) 632–635.
[42] F. Simpson, Intensity and direction of lattice-preferred orientation of olivine: are electrical and seismic anisotropies of the Australian mantle reconcilable?, Earth Planet. Sci. Lett. 203 (2002) 535–547.
[43] J. Trampert, J.H. Woodhouse, Global anisotropic phase velocity maps for fundamental mode surface waves between 40 and 150 seconds, Geophys. J. Int. (2003) in press.
[44] F.J. Simons, R.D. van der Hilst, M.T. Zuber, Spatio-spectral localization of isostatic coherence anisotropy in Australia and its relation to seismic anisotropy: Implications for lithospheric deformation, J. Geophys. Res. 108 (2003) 10.1029/2001JB000704.
[45] R.D. van der Hilst, B.L.N. Kennett, D. Christie, J. Grant, Project SKIPPY explores the lithosphere and mantle beneath Australia, EOS Trans. AGU 75 (1994) 177–181.
[46] A. Zielhuis, R.D. van der Hilst, Upper-mantle shear velocity beneath eastern Australia from inversion of waveforms from SKIPPY portable arrays, Geophys. J. Int. 127 (1996) 1–16.
[47] F.J. Simons, A. Zielhuis, R.D. van der Hilst, The deep structure of the Australian continent from surface-wave tomography, Lithos 48 (1999) 17–43.
[48] G. Nolet, Partitioned waveform inversion and two-dimensional structure under the Network of Autonomously Recording Seismographs, J. Geophys. Res. 95 (1990) 8499–8512.

[49] G. Clitheroe, Ó. Guðmundsson, B.L.N. Kennett, The crustal thickness of Australia, J. Geophys. Res. 105 (2000) 13697–13713.
[50] J.-P. Montagner, Surface waves on a global scale, Influence of anisotropy and anelasticity, in: E. Boschi, G. Ekström, A. Morelli (Eds.), Seismic Modelling of Earth Structure, Ed. Compositori, Bologna, 1996, pp. 81–148.
[51] J.-P. Montagner, H.-C. Nataf, A simple method for inverting the azimuthal anisotropy of surface waves, J. Geophys. Res. 91 (1986) 511–520.
[52] G. Clitheroe, R.D. van der Hilst, Complex anisotropy in the Australian lithosphere from shear-wave splitting in broad-band *SKS*-records, in: J. Braun, J.C. Dooley, B. Goleby, R.D. van der Hilst, C. Klootwijk (Eds.), Structure and Evolution of the Australian Continent, AGU Geodyn. Ser. 26, Washington, DC, 1998, pp. 73–78.
[53] S. Özalaybey, W.P. Chen, Frequency-dependent analysis of *SKS-SKKS* waveforms observed in Australia: Evidence for null birefringence, Phys. Earth Planet. Inter. 114 (1999) 197–210.
[54] D.L. Turcotte, G. Schubert, Geodynamics, Application of Continuum Physics to Geological Problems, Wiley, New York, 1982.
[55] D.W. Forsyth, Subsurface loading and estimates of the flexural rigidity of continental lithosphere, J. Geophys. Res. 90 (1985) 12623–12632.
[56] F.J. Simons, R.D. van der Hilst, Age-dependent seismic thickness and mechanical strength of the Australian lithosphere, Geophys. Res. Lett. 29 (2002) 1529, 10.1029/2002GL014962.
[57] F.J. Simons, M.T. Zuber, J. Korenaga, Isostatic response of the Australian lithosphere: Estimation of effective elastic thickness and anisotropy using multitaper spectral analysis, J. Geophys. Res. 105 (2000) 19163–19184.
[58] A. Vauchez, A. Tommasi, G. Barruol, Rheological heterogeneity, mechanical anisotropy and deformation of the continental lithosphere, Tectonophysics 296 (1998) 61–86.
[59] A. Tommasi, A. Vauchez, Continental rifting parallel to ancient collisional belts; An effect of the mechanical anisotropy of the lithospheric mantle, Earth Planet. Sci. Lett. 185 (2001) 199–210.
[60] P.G. Silver, W.E. Holt, The mantle flow field beneath Western North America, Science 295 (2002) 1054–1057.
[61] S. Ji, S. Rondenay, M. Mareschal, G. Sénéchal, Obliquity between seismic and electrical anisotropies as a potential indicator of movement sense for ductile shear zones in the upper mantle, Geology 24 (1996) 1033–1036.
[62] K. Lambeck, Structure and evolution of the intracratonic basins of central Australia, Geophys. J. R. Astron. Soc. 74 (1983) 843–886.
[63] M. Sandiford, M. Hand, Controls on the locus of intraplate deformation in central Australia, Earth Planet. Sci. Lett. 162 (1998) 97–110.
[64] A. Lenardic, L. Moresi, H. Mühlhaus, The role of mobile belts for the longevity of deep cratonic lithosphere: The crumple zone model, Geophys. Res. Lett. 27 (2000) 1235–1238.
[65] K. Lambeck, G. Burgess, R.D. Shaw, Teleseismic traveltime anomalies and deep crustal structure in central Australia, Geophys. J. Int. 94 (1988) 105–124.
[66] A.B. Watts, Isostasy and Flexure of the Lithosphere, Cambridge Univ. Press, Cambridge, 2001.
[67] A. Meltzer, R. Rudnick, P. Zeitler, A. Levander, G. Humphreys, K. Karlstrom, E. Ekstrom, C. Carlson, T. Dixon, M. Gurnis, P. Shearer, R.D. van der Hilst, The USArray initiative, GSA Today 9 (1999) 8–10.
[68] A. Zielhuis, G. Nolet, Shear-wave velocity variations in the upper-mantle beneath central Europe, Geophys. J. Int. 117 (1994) 695–715.
[69] G. Ekström, Mapping the lithosphere and asthenosphere with surface waves: Lateral structure and anisotropy, in: M.A. Richards, R.G. Gordon, R.D. van der Hilst (Eds.), The History and Dynamics of Global Plate Motions, AGU Geophys. Monogr. 121, Washington, DC, 2000, pp. 239–255.
[70] F.J. Simons, Structure and evolution of the Australian continent: Insights from seismic and mechanical heterogeneity and anisotropy, Ph.D. thesis, M.I.T., Cambridge, MA (June 2002).
[71] L. Boschi, G. Ekström, New images of the Earth's upper mantle from measurements of surface wave phase velocity anomalies, J. Geophys. Res. B 107 (2002) 2059, 10.1029/2000JB000059.
[72] I. Daubechies, Time-frequency localization operators: A geometric phase space approach, IEEE Trans. Inform. Theory 34 (1988) 605–612.
[73] S. Olhede, A.T. Walden, Generalized morse wavelets, IEEE Trans. Signal Process. 50 (2002) 2661–2670.

Appendix

A Inversion for azimuthal anisotropy

This first appendix summarizes a few key points treated in more detail in [37].

For each of the paths $p = 1, ..., M$ a waveform fit results in a set of $K(p)$ depth-dependent constraints. These individual constraints are uncorrelated: this is achieved explicitly by the diagonalization of their error covariance matrix [68]. By themselves modal Fréchet kernels are not orthogonal, so phase velocity measurements in a particular frequency band [69] cannot be converted into depth-dependent shear velocity models without this extra step [37]. In the formalism of [68] every seismogram yields a set of uncorrelated depth-distributed averages of the three-dimensional wavespeed structure:

$$q_k^p = \int_{P_p} \langle G_k^p(r) |\, \delta\beta(r, \theta, \varphi) \rangle \; d\Delta. \qquad \text{(A.1)}$$

Here, $k = 1, ..., K(p)$ indexes the number of independent constraints that have been retained after applying an error cut-off criterion (discussed by [70]), and $d\Delta$ indicates the incremental epicentral distance along the great circle path P_p. The "data" q_k^p have been scaled to unit variance. We've used the notation: $\langle f|g \rangle \equiv \int_0^a f(r)g(r)dr$, where the integration goes from the center ($r = 0$) to the surface ($r = a$) of the Earth. The 3-D shear wave speed anomaly is denoted as $\delta\beta(\mathbf{r}) = \delta\beta(r, \theta, \varphi)$ and $G_k^p(r)$ is a kernel function which indicates how the data constraint q_k^p is related to the model parameters $\delta\beta$.

The precise form of $G_k^p(r)$ is determined by the error structure of the parameters determined in the nonlinear waveform inversion; practically, as more (and better) information is available on the velocity structure, the total number k increases to some number $K(p)$ for a particular path. Insofar as this information is constrained by higher modes or lower-frequency fundamental modes of the seismogram, the sensitivity of the kernel $G_k^p(r)$ will shift to deeper structure as k increases. The value of q_k^p is influenced by the local path reference model that was used in obtaining the fit [71]; the velocity anomaly is with respect to a regional 1-D background model common to all paths.

The velocity anomalies are expanded onto a set of equal-area surface cells parameterized as $l_t(\theta, \varphi)$ for $t = 1, ..., T$ where $l_t(\theta, \varphi) = 1$ if the horizontal coordinates (θ, φ) are inside the cell, and 0 elsewhere. The radial basis functions are denoted as $h_j(r), j = 1, ..., J$; they can be discrete layers or high-order splines, but are here taken to be boxcar (at the crustal, 400 and 670 km discontinuities) and tent functions (interpolating between nodes at 15, 30, 80, 140, 200 and 300 km). The surface and depth parameterization describe a set of basis functions $s_i(\mathbf{r}) = l_t(\mathbf{r}/r)\, h_j(r)$, with $i = 1, ..., N$ and $N = TJ$ upon which to expand $\delta\beta(\mathbf{r})$ as $\delta\beta(\mathbf{r}) = \sum_i^N b_i s_i(\mathbf{r})$. Inserting these definitions into Eq. A.1 we obtain [70]:

$$q_k^p = \sum_i^N b_i \, L_t^p \, \langle G_k^p(r) | h_j(r) \rangle \; . \qquad \text{(A.2)}$$

We've introduced L_t^p, the path length of path p in surface cell t. All k constraints of one path sample the same cells on the surface, but the depth-averaging functions differ.

Defining $\mathcal{G}$ to be dependent on the path lengths in the surface cells and on the sensitivity to depth structure which is influenced by the mode structure of the seismogram and the diagonalized error covariance matrix of the waveform inversion, we may write:

$$q_k^p = \sum_i^N \mathcal{G}_{ki}^p b_i \quad \text{or} \quad \mathbf{q} = \mathcal{G} \cdot \mathbf{b}. \qquad \text{(A.3)}$$

The dimensions of the matrices involved are $[\mathbf{q}] = \sum_{p=1}^M K(p) \times 1$, $[\mathbf{G}] = \sum_{p=1}^M K(p) \times N$, and $[\mathbf{b}] = N \times 1$.

B Hermite multispectrogram analysis

This second appendix summarizes a few key points treated in more detail in [44].

For two spatially variable (non-stationary) random processes $\{G\}$ (gravity) and $\{H\}$ (topography), defined on $\mathbf{r} = (x, y)$ in the spatial domain and on $\mathbf{k} = (k_x, k_y)$ in the Fourier domain, the coherence-square function relating both fields, γ^2_{GH}, is defined as the ratio of their cross-spectral density, S_{GH}, normalized by the individual power spectral densities, S_{GG} and S_{HH}:

$$\gamma^2_{GH}(\mathbf{r}, \mathbf{k}) = \frac{|S_{GH}(\mathbf{r}, \mathbf{k})|^2}{S_{GG}(\mathbf{r}, \mathbf{k}) S_{HH}(\mathbf{r}, \mathbf{k})}. \tag{B.1}$$

An estimate $\hat{S}$ of the spectral density function is obtained by taking a weighted average of N windowed periodograms:

$$\hat{S}_{GG}(\mathbf{r}, \mathbf{k}) = \left(\sum_{n=0}^{N-1} \lambda_n \right)^{-1} \times \sum_{n=0}^{N-1} \lambda_n \left| \int h_n(\boldsymbol{\tau} - \mathbf{r}) G(\boldsymbol{\tau}) e^{-i2\pi \mathbf{k} \cdot \boldsymbol{\tau}} \, d\boldsymbol{\tau} \right|^2. \tag{B.2}$$

with data windows h_n and weights λ_n. The integration is implemented discretely by the Fast Fourier Transform algorithm. The properties of the windows and weights determine the resolution and variance of the estimate. Maximal, symmetric concentration in the space-wavenumber domain [72,73] is obtained by using data windows that are Hermite polynomials (calculated by recursion), modulated by the Gaussian:

$$h_n(x) = \frac{H_n(x) e^{-x^2/2}}{\pi^{1/4} \sqrt{2^n n!}}. \tag{B.3}$$

The weights are given by:

$$\lambda_n(R) = \frac{1}{n!} \gamma(R^2/2, n + 1), \tag{B.4}$$

where γ denotes the incomplete gamma function. We used $R = 3$ and $N = R^2$ windows in each dimension. The parameter R regulates the resolution of the spectral estimate. As it is the radius of a spherical domain in the space-wavenumber phase plane, spatial resolution is not traded off with spectral resolution, and no spurious anisotropy is introduced by combining dimensions. This is the main advantage over conventional multi-taper methods with Slepian functions as windows, which are not designed to capture spatial variations and must assume local stationary instead. We sampled the spatial domain at points about 500 km apart [44].

The data windows h_n are eigenfunctions of a spatio-spectral concentration operator, with eigenvalues λ_n. To study multi-dimensional processes, windows are formed by taking the outer product of all pairs of 1-D functions, and the eigenvalues by multiplication. Eq. B.4 shows the latter can be calculated cheaply without actually solving the concentration eigenvalue problem. This is responsible for the speed advantage of the method compared to the Slepian multitaper method.

With orthonormal data windows the individual spectral estimates are approximately uncorrelated and the variance of the coherence estimate $\hat{\gamma}^2$ decreases with the number of windows. In function of the true coherence γ^2, this variance is given by

$$\sigma^2\{\hat{\gamma}^2\} = 2\gamma^2 \frac{(1 - \gamma^2)^2}{N}. \tag{B.5}$$

However, the $\sim 1/N$ decrease in the estimation variance is achieved at the expense of widening the concentration region $R = \sqrt{N}$, which degrades the spectral resolution. The errors quoted will be the square root of the average estimation variance divided by the square root of the number of points estimated on a line with constant azimuth through the center of the spectrum. In [44] we assess the significance of the minima by comparing the separation of azimuthal profiles of coherence in “weak” and “strong” directions with their errors.